The Astrophysical Journal, 995:54 (14pp), 2025 December 10 https://doi.org/10.3847/1538-4357/ae17b0

A Late-time Radio Survey of Type Ia-CSM Supernovae with the Very Large Array

Olivia Griffith[1], Grace Showerman[1], Sumit K. Sarbadhicary[2,3,4,5], Chelsea E. Harris[1], Laura Chomiuk[1], Jesper Sollerman[6], Peter Lundqvist[6], Javier Moldón[7], Miguel Pérez- Torres[7,8], Erik C. Kool[6,9,10], and Takashi J. Moriya[11,12,13]
[1] Center for Data Intensive and Time Domain Astronomy, Department of Physics and Astronomy, Michigan State University, East Lansing, MI 48824, USA; oliviagriffith21@gmail.com
[2] Department of Physics, The Ohio State University, Columbus, OH 43210, USA
[3] Center for Cosmology & Astro-Particle Physics, The Ohio State University, Columbus, OH 43210, USA
[4] Department of Astronomy, The Ohio State University, Columbus, OH 43210, USA
[5] Department of Physics and Astronomy, The Johns Hopkins University, Baltimore, MD 21218, USA
[6] The Oskar Klein Centre, Department of Astronomy, Stockholm University, AlbaNova, SE-10691, Stockholm, Sweden
[7] CSIC, Instituto de Astrofísica de Andalucía, Glorieta de la Astronomía S/N, E-18008, Granada, Spain
[8] School of Sciences, European University Cyprus, Diogenes street, Engomi, 1516 Nicosia, Cyprus
[9] Finnish Centre for Astronomy with ESO (FINCA), University of Turku, 20014 Turku, Finland
[10] Department of Physics and Astronomy, University of Turku, 20014 Turku, Finland
[11] National Astronomical Observatory of Japan, National Institutes of Natural Sciences, 2-21-1 Osawa, Mitaka, Tokyo 181-8588, Japan
[12] Graduate Institute for Advanced Studies, SOKENDAI, 2-21-1 Osawa, Mitaka, Tokyo 181-8588, Japan
[13] School of Physics and Astronomy, Monash University, Clayton, VIC 3800, Australia
Received 2025 June 23; revised 2025 October 21; accepted 2025 October 23; published 2025 December 4

Abstract

Type Ia-CSM supernovae (SNe) are a rare and peculiar subclass of thermonuclear SNe characterized by emission lines of hydrogen or helium, indicative of high-density circumstellar medium (CSM). Their implied mass-loss rates of $\sim 10^{-4}$–$10^{-1}\ M_{\odot}\ \mathrm{yr}^{-1}$ (assuming $\sim 100\ \mathrm{km\ s}^{-1}$ winds) from optical observations are generally in excess of values observed in realistic SN Ia progenitors. In this paper, we present an independent study of CSM densities around a sample of 29 archival Ia-CSM SNe using radio observations with the Karl G. Jansky Very Large Array at 6 GHz. Motivated by the late ($\sim$2 yr) radio detection of the Ia-CSM SN 2020eyj, we observed old (>1 yr) SNe, when we are more likely to see the emergent synchrotron emission that may have been suppressed earlier by free–free absorption by the CSM. We do not detect radio emission down to 3σ limits of $\sim$35 μJy in our sample. The only radio-detected candidate in our sample, SN 2022esa, was likely misclassified as a Ia-CSM with early spectra, and appears more consistent with a peculiar Ic based on later epochs. Assuming wind-like CSM with temperatures between 2×10^4 K and 10^5 K, and a magnetic field-to-shock energy fraction $\epsilon_B = 0.01 - 0.1$, the radio upper limits rule out mass-loss rates between $\sim 10^{-4}$ and $10^{-2}\ M_{\odot}\ \mathrm{yr}^{-1}\ (100\ \mathrm{km\ s}^{-1})^{-1}$. This is somewhat in tension with the estimates from optical observations, and may indicate that more complex CSM geometries and/or lower values of ϵ_B may be present.

Unified Astronomy Thesaurus concepts: Circumstellar matter (241); Type Ia supernovae (1728); White dwarf stars (1799); Radio astronomy (1338)

Materials only available in the online version of record: machine-readable tables

1. Introduction

The progenitor scenario(s) for Type Ia supernovae (SNe Ia) remains one of the biggest open questions in astrophysics. The two broad scenarios explored by the community have been the single-degenerate scenario, involving a white dwarf accreting from a nondegenerate main-sequence star, red giant, or helium star companion (e.g., J. Whelan & I. J. Iben 1973; K. Nomoto 1982), and the double-degenerate scenario, involving two white dwarfs in a binary system (e.g., A. V. Tutukov & L. R. Yungelson 1979; I. Iben & A. V. Tutukov 1984; R. F. Webbink 1984; K. J. Shen et al. 2018). Unfortunately, observations have yet to establish which combination of these scenarios are contributing to the observed SN Ia population in the Universe (see, e.g., S. W. Jha et al. 2019; Z.-W. Liu et al. 2023; A. J. Ruiter & I. R. Seitenzahl 2025, for recent reviews). Considering the importance of SNe Ia as the primary producers of Fe-group elements (C. M. Raiteri et al. 1996), as drivers of chemical enrichment in the Universe (F. Matteucci & S. Recchi 2001), and as standard candles (e.g., I. P. Pskovskii 1977; M. M. Phillips 1993) for precise astrophysical distance measurements (M. M. Phillips 1993; A. G. Riess et al. 1998; S. Perlmutter et al. 1999; M. M. Phillips et al. 1999; C. R. Burns et al. 2018), the resolution of the SN Ia progenitor problem remains a high-priority goal for our field.

Here we focus on a particularly intriguing and rare subclass of SNe Ia that have eluded explanation: SNe Ia-CSM (J. M. Silverman et al. 2013). They are characterized by strong narrow emission lines of hydrogen, which have been attributed to circumstellar material (CSM) produced by mass-loss from the progenitor. SNe Ia-CSM also appear to be more luminous than normal SNe Ia, and have a preference for star-forming host galaxies (Y. Sharma et al. 2023). They have been considered strong candidates for the single-degenerate channel, since white dwarfs with red giant or asymptotic giant branch (AGB) star companions can have strong winds (e.g., Z. Han & P. Podsiadlowski 2006; B. Dilday et al. 2012). Some well-known examples of Ia-CSM SNe include PTF11kx (B. Dilday et al. 2012), SN 2002ic (M. Hamuy et al. 2003), and SN 2005gj (G. Aldering et al. 2006). Many of them were

previously confused with Type IIn SNe owing to dilution and blending of key spectral features by the bright continuum (O. D. Fox et al. 2015; G. Leloudas et al. 2015; C. Inserra et al. 2016). In very rare cases, CSM interaction can appear at late times in SNe Ia due to distant, detached shells of CSM (e.g., M. L. Graham et al. 2019; L. Wang et al. 2024; G. Mo et al. 2025; J. H. Terwel et al. 2025).

A major conundrum for SNe Ia-CSM is that their implied mass-loss rates from the hydrogen emission lines are typically in the range of 10^{-4}–$10^{-2}\,M_{\odot}\,\mathrm{yr}^{-1}$ (assuming wind velocities of $100\,\mathrm{km\,s}^{-1}$; e.g., G. Aldering et al. 2006; B. Dilday et al. 2012; J. M. Silverman et al. 2013; Y. Sharma et al. 2023). These are 2–4 orders of magnitude higher than observed in realistic single-degenerate progenitors with the highest mass-loss rates, such as symbiotic systems with AGB companions (e.g., E. R. Seaquist & A. R. Taylor 1990; E. R. Seaquist et al. 1993; L. Chomiuk et al. 2012a). Other scenarios, such as dense shells of swept-up mass from recurrent novae (e.g., K. Moore & L. Bildsten 2012; M. J. Darnley et al. 2019) or common-envelope shells preceding formation of double-degenerate systems (e.g., M. Livio & A. G. Riess 2003), have also been invoked, but a clear connection between observations and progenitors is lacking so far for SNe Ia-CSM.

An orthogonal way of studying CSM properties is with radio observations, which trace synchrotron emission from SN shocks interacting with the ambient medium (R. A. Chevalier 1982). Given the observed luminosity or upper limits, and some assumptions about the fractional shock energy shared with the electrons and magnetic fields, reasonable estimates of the CSM density can be obtained. While radio emission has been observed in many core-collapse SNe interacting with the dense CSM around their massive progenitors (e.g., K. W. Weiler et al. 2002; R. A. Chevalier et al. 2006; A. M. Soderberg et al. 2012), similar emission has been elusive in Type Ia SNe. Their nondetections have provided strong evidence that most SNe Ia have low-density environments, ruling out symbiotic companions, and even a substantial parameter space of nova-driven and accretion-disk-driven winds (e.g., N. Panagia et al. 2006; L. Chomiuk et al. 2012b, 2016; A. Horesh et al. 2012; P. Lundqvist et al. 2020; C. E. Harris et al. 2023).

In contrast to the general SN Ia population, there are fewer constraining radio observations of Ia-CSM SNe. L. Chomiuk et al. (2016) carried out the largest radio survey of SNe Ia, in which there were six Ia-CSM SNe that all showed nondetections. However, these observations were generally taken within a few months of the explosion, and therefore could have missed the radio emission due to synchrotron self-absorption and free–free absorption by the ionized CSM. This is clearly seen in radio observations of their closest counterparts, Type IIn SNe, whose radio light curves peak a few years after explosion (P. Chandra 2018; M. F. Bietenholz et al. 2021; I. Sfaradi et al. 2025). Unfortunately, very few late-time radio observations of SNe Ia-CSM exist on these timescales to detect emission and independently constrain the properties of the high-density CSM.

In this paper, we present the first and largest "late-time" (i.e., >1 yr after explosion) radio survey of SNe Ia-CSM with the Karl G. Jansky Very Large Array (VLA). The survey was inspired by the discovery of radio emission from the He-rich Ia-CSM SN 2020eyj, which at a distance of $\sim$131 Mpc produced bright radio emission ($\sim 10^{27}$ erg s^{-1} Hz^{-1}) at 5–6 GHz on timescales of $\sim$1.5–2 yr after explosion (E. C. Kool et al. 2023). This is the first and only thermonuclear SN to date with detected radio emission and, together with the late-time radio emission in Type IIn SNe (M. F. Bietenholz et al. 2021), encourages a similar search of Ia-CSM SNe sufficiently late in time to detect any emergent emission. Here we target 29 archival SNe Ia-CSM with ages of at least 1 yr, and analyze them with synchrotron emission models of interaction with a $\rho \propto r^{-2}$ windlike CSM in order to obtain constraints on their mass-loss rates, enabling comparison with values deduced from optical observations.

The paper is organized as follows. Section 2 describes the VLA observations of our 29 targets. Section 3 discusses the radio light-curve model used for deriving mass-loss rates (or upper limits) from the observed luminosities. Section 4 goes over the results of our observations and measurements of mass-loss rates, and Section 5 discusses these in the context of mass-loss rate measurements from other wavelengths, and briefly considers the detectability of shell-like CSM. We conclude in Section 6.

2. Observations

In this section, we describe the radio observations conducted on our SN Ia-CSM sample. We observed 29 SNe Ia-CSM at 6 GHz with the VLA in the A configuration during 2023 July–August as part of the program VLA/23A-328 (PI: Sarbadhicary). The sample was selected from published SNe Ia-CSM in J. M. Silverman et al. (2013) and O. D. Fox et al. (2015), and transients classified as "Ia-CSM" in the Transient Name Server (TNS) for SNe Ia discovered after 2016. We excluded SNe Ia-CSM that are outside the decl. limit of the VLA, selecting targets at $\delta > -35^{\circ}$. Our final sample consists of SNe with ages of 1–25 yr, which are located at distances ranging from 90 to 900 Mpc (Table 1). These distances were calculated with the redshift values given in the TNS along with the assumption of $H_0 = 70$ km s^{-1} Mpc^{-1}.

Our targets were primarily observed for 10 minute durations (a few distant ones for 20 or 30 minutes) in the C band (4–8 GHz) using continuum mode, which covers the entire 4 GHz of bandwidth with 2 MHz-wide channels. Observations were obtained in the A configuration to achieve good localization accuracy (with restoring beams of $\sim 0\farcs3$) and diminish the effects of diffuse emission from the SN host galaxies. Each target was observed between complex gain calibration observations lasting 1–2 minutes using calibrators that were selected for their brightness, high positional accuracy, and proximity to each respective target. Flux calibrations lasting $\sim$8 minutes were done at the beginning of each observing block using one of the following of the VLA's primary calibrators: 3C286, 3C138, 3C48, or 3C147.

We imaged and measured radio flux densities (or upper limits) for all of the targets in the sample using standard calibration and imaging procedures for radio continuum data followed in previous papers (e.g., L. Chomiuk et al. 2016; C. E. Harris et al. 2023; G. Hosseinzadeh et al. 2023). We used the standard VLA calibration pipeline implemented in `CASA` version 6.4.1.12 (CASA Team et al. 2022) for reducing the continuum data from these observations. The pipeline applied online flags reported during observation, and additional flagging of radio-frequency interference (RFI) was done with the `rflag` algorithm. The pipeline performed iterative flagging–calibration cycles on the raw visibility data. The primary calibrators were used for delay, bandpass, and absolute flux density calibration, while the secondary

Table 1
Radio Observations of Our SN Ia-CSM Sample

SN Name	Discovery Date (UT)	Observation Date (UT)	Time Since Explosion (yr)	R.A. (J2000) (h:m:s)	Decl. (J2000) (deg: arcmin: arcsec)	Distance (Mpc)	3σ Flux Upper Limit (μJy)	3σ Luminosity Upper Limit (10^{27} erg s^{-1} Hz^{-1})
SN 1999E	99/01/15	23/08/20	24.6	13:17:16.37	−18:33:13.4	109.1	<36	<0.52
SN 2002ic	02/11/13	23/08/28	20.8	01:30:02.55	21:53:06.9	296.8	<29	<3.1
SN 2008cg	08/05/05	23/08/25	15.3	15:54:15.15	10:58:25.0	159.3	<41	<1.3
SN 2009in	09/08/25	23/08/27	14.0	23:22:35.32	−13:05:43.6	103.3	<33	<0.43
PTF10htz	10/04/03	23/08/16	13.4	13:08:37.52	79:47:13.2	153.9	<48	<1.4
SN 2011dz	11/06/26	23/08/25	12.2	16:12:44.82	28:17:03.2	106.9	<37	<0.51
SN 2011jb	11/11/28	23/08/13	11.7	11:37:04.80	15:28:14.2	382.5	<34	<5.9
CSS120327	12/03/27	23/08/20	11.4	11:05:20.08	−01:52:05.2	415.4	<39	<8.0
SN 2013dn	13/06/14	23/08/27	10.2	23:37:45.74	14:42:37.1	250.9	<30	<2.2
SN 2014T	14/02/22	23/08/25	9.5	14:36:04.98	02:20:34.2	411.5	<33	<6.7
SN 2014Y	14/03/02	23/07/30	9.4	07:23:33.38	54:26:19.8	172.0	<28	<0.99
SN 2014ab	14/03/09	23/08/20	9.5	13:48:05.99	07:23:16.4	101.2	<40	<0.50
SN 2016iks	16/11/20	23/08/27	6.8	23:07:21.53	02:54:28.2	282.7	<26	<2.5
SN 2016jae	16/12/22	23/08/13	6.6	09:42:34.51	10:59:35.4	91.4	<36	<0.36
SN 2017eby	17/04/01	23/08/25	6.4	14:38:50.74	14:44:26.0	368.1	<30	<4.9
SN 2017ifu	17/10/28	23/08/28	5.8	02:50:55.03	−02:08:06.4	887.8	<24	<23
SN 2017hzw	17/11/13	23/07/30	5.7	02:05:18.13	53:12:13.4	226.9	<30	<1.9
SN 2018cqj	18/06/13	23/08/13	5.2	09:40:21.46	−06:59:19.8	91.4	<36	<0.37
SN 2018gkx	18/09/08	23/08/16	4.9	13:52:19.22	55:38:28.3	646.0	<33	<17
SN 2019agi	19/01/25	23/08/25	4.6	16:22:43.99	24:01:09.7	268.7	<59	<5.1
SN 2019rvb	19/10/02	23/08/26	3.9	16:38:10.16	68:27:49.1	890.5	<26	<25
SN 2020kre	20/05/21	23/08/20	3.3	13:10:29.87	−01:18:51.1	640.9	<77	<38
SN 2020onv	20/07/11	23/08/27	3.1	23:16:46.02	−23:18:37.1	435.8	<38	<8.6
SN 2020qxz	20/08/08	23/08/16	3.0	18:04:00.23	74:00:50.3	442.7	<30	<7.0
SN 2020abfe	20/11/14	23/08/26	2.8	20:00:03.31	10:09:04.2	426.1	<42	<9.2
SN 2020aeur	20/12/22	23/08/13	2.6	09:26:20.39	01:52:43.9	226.9	<37	<2.3
SN 2020aekp	20/12/27	23/08/26	2.7	15:43:11.39	17:48:47.2	236.1	<49	<3.3
SN 2022erq	22/03/11	23/08/16	1.4	18:33:25.36	44:05:11.7	296.8	<32	<3.4
SN 2022esa	22/03/12	23/08/26	1.5	16:53:57.60	−09:42:10.3	100.2	1129 ± 52	13.6 ± 0.6
SN 2022esa	22/03/12	24/10/19	2.6	16:53:57.60	−09:42:10.3	100.2	799 ± 36	9.6 ± 0.4

Note. Measurements represent peak flux density for SN 2022esa using CASA `imfit` (see Sections 2 and 4).

(This table is available in its entirety in machine-readable form in the online article.)

calibrator was used for antenna-based complex gain calibrations. After the pipeline ran, each calibrated dataset was manually inspected and flagged for any remaining RFI.

Imaging was performed using the `tclean` task in `CASA`. We used `gridder=wproject` to mitigate the impact of non-coplanar baselines and sky curvature during wide-field imaging. For deconvolution, we used multiterm multi-frequency synthesis with `nterms=2` to account for frequency-dependent brightness in the imaging field. We applied Briggs weighting with `robust=0` to balance point-source sensitivity with sidelobe contamination in our observations. We created images 6000 pixels wide, at a pixel scale of $0\farcs07$, which is approximately one-fifth of the synthesized beamwidth in the VLA *C* band and A configuration. We cleaned our images for a maximum of 10^4 iterations or until the image rms contrast was less than 5 times the peak residual (`nsigma=5`). No self-calibration was necessary as our final images were close to the expected noise limit, with no artifacts from bright sources.

For each object in our sample, we recorded the pixel flux density and the 3σ rms noise at the location of the SN. Most of the SNe were nondetections, so we recorded 3σ upper limits at 6 GHz, defined as the flux density at the SN location plus the 3σ rms noise in the 50×50 pixel region around the SN. If the flux density at the SN location was negative, we considered the 3σ rms noise as the upper limit.

The majority of our sources turned out to be nondetections down to the 3σ limits of $\lesssim$35 μJy reported in Table 1. The implications of these nondetections regarding progenitor mass-loss rates are discussed in Section 4. One of our SNe, 2022esa, did produce detectable radio emission of $\sim$1.1 mJy, although, as we discuss in Section 4, the TNS classification of this object as a Ia-CSM is likely dubious. In order to confirm that the radio emission at the location of SN 2022esa is transient in nature, we obtained follow-up observations in the same frequency and array configuration as part of VLA/24B-381. The dataset was flagged, calibrated, and imaged following the same procedure as the VLA/23A-328 datasets discussed above. We additionally recorded the peak flux density of the point source in both images using elliptical Gaussian fitting with the `CASA` task `imfit`. Indeed, the flux density of the source decreased to 0.8 mJy after a year, corresponding to a 30% decrease. These measurements are also presented in Table 1, and implications of the detections are further discussed in Section 4.

3. Radio Light-curve Model

In this section, we describe our model of synchrotron radio emission due to interaction with a windlike CSM, which will

be used to constrain the mass-loss rates of our SN Ia-CSM sample in Section 4, given upper limits on their 6 GHz radio emission obtained in Section 2.

3.1. Synchrotron Emission

We roughly follow the same synchrotron emission modeling procedure for Type Ia SNe that was used in previous papers (e.g., L. Chomiuk et al. 2012b, 2016; C. E. Harris et al. 2023; G. Hosseinzadeh et al. 2023), with a few modifications to the shock dynamics described in Section 3.2. We refer the reader to these papers for details of the model, but include a brief description here.

The model follows the classical R. A. Chevalier (1982) model of synchrotron emission from SN ejecta interacting with CSM. The density profile of the CSM is assumed to be windlike, with $\rho = \dot{M}/4\pi r^2 v_{\rm wind}$, where $\dot{M}$ is the wind's constant mass-loss rate, and $v_{\rm wind}$ is the wind velocity. Although idealized, a windlike CSM is a reasonable approximation for single-degenerate progenitors with red giant or AGB companions that are continuous mass-losing systems, and are considered strong candidates for our Ia-CSM SNe. Previous radio studies of SNe have often assumed a windlike CSM since it provides convenient, self-similar solutions for shock dynamics and the resulting radio light curves, making it possible to explore a vast parameter space of CSM properties (see examples in R. A. Chevalier & C. Fransson 2017). Finally, a CSM wind profile is generally the model assumed in optical studies of Ia-CSM SNe for estimation of mass-loss rates (see discussion in Section 5), so we assume the same for consistency with our radio-based results.

Broadly speaking, the optically thin synchrotron luminosity depends on the volume of the shock, the energy density in the amplified magnetic field, and the energy density in relativistic electrons. This electron population is assumed to have a characteristic power-law spectrum, $N(E) = N_0 E^{-p}$, where we assume $p = 3$ that is commonly observed in Type Ib/c SNe (A. M. Soderberg et al. 2005, 2006) and is often assumed for Type Ia SNe (L. Chomiuk et al. 2016). The resulting optically thin luminosity will have a frequency dependence $\propto \nu^{-1}$. The energy density in relativistic electrons is assumed to be equal to $\epsilon_e \rho v_s^2$, where ϵ_e is the fraction of the shock energy in the relativistic electrons, ρ is the density of CSM that the shock is interacting with at the time of radio observation, and v_s is the shock velocity. The amplified magnetic field is assumed to scale with the shock energy as $\boldsymbol{B^2 = 8\pi\epsilon_B \rho v_s^2}$ (L. Chomiuk & E. M. Wilcots 2009; T. A. Thompson et al. 2009), where ϵ_B, analogous to ϵ_e, is the fraction of shock energy in the amplified magnetic field. At early times, we assume this emission will be suppressed by synchrotron self-absorption and free–free absorption by the dense CSM. For synchrotron self-absorption, we use the form of the radio spectrum laid out in R. A. Chevalier (1998) that self-consistently accounts for a $L_\nu \propto \nu^{2.5}$ turnover at lower frequencies, where the self-absorption optical depth >1. For free–free absorption, we multiply the luminosity by a factor $\epsilon^{-\tau_{\rm ff}}$, where $\tau_{\rm ff}$ is the free–free optical depth at a given wavelength (λ), which we derive from Equation (2.3) of C. Fransson et al. (1996) as

$$\tau_{\rm ff} \approx 0.46\, \lambda^2 \left(\frac{\dot{M}_{-5}}{v_{\rm wind,10}}\right)^2 T_5^{-3/2}\, v_{s,4}^{-3} \left(\frac{t}{11.57d}\right)^{-3}, \quad (1)$$

where $\dot{M}_{-5}$ is the mass-loss rate in units of $10^{-5}\, M_\odot\, {\rm yr}^{-1}$, $v_{\rm wind,10}$ is the wind velocity in units of $10\, {\rm km\, s^{-1}}$, T_5 is the wind temperature in 10^5 K, $v_{s,4}$ is the shock velocity in $10^4\, {\rm km\, s^{-1}}$, and t is the time elapsed between SN explosion and the radio observation in question.

Our goal is to obtain constraints on the mass-loss rate given the observed radio luminosity (or upper limit) for each SN, but these constraints will depend on the values of several tunable parameters in our model. Based on C. E. Harris et al. (2023), the parameters expected to have the largest impact on the interpretation of the radio upper limits are ϵ_B, ϵ_e, and $T_{\rm wind}$. As per convention, we assume the range of $\epsilon_B = 0.01$–0.1 (L. Chomiuk et al. 2012b), while keeping $\epsilon_e = 0.1$ for every model (see Section 5 for a discussion of these ranges). The values for $T_{\rm wind}$ are expected to vary between 2×10^4 K and 10^5 K for windlike CSM around SNe (P. Lundqvist et al. 2013). In reality, both parameters will likely vary with time as the shock slows down and the postshock conditions change, but, for simplicity, we discuss our results for different constant values of $T_{\rm wind}$ and ϵ_B (Table 2) in order to provide an idea of the extent to which the various parameters affect the shape of the light curve, and therefore how they change the corresponding mass-loss rates.

Table 2
Parameter Values of the Different Radio Light-curve Models for Windlike CSM Explored in This Paper

	Model A	Model B	Model C
ϵ_B	0.1	0.1	0.01
$T_{\rm wind}$ (K)	10^5	2×10^4	2×10^4
ϵ_e	0.1	0.1	0.1
$v_{\rm wind}$ (km s^{-1})	100	100	100
ν (GHz)	6	6	6

The synchrotron luminosity, corrected for absorption, is estimated using the equations detailed in R. A. Chevalier (1998) and L. Chomiuk et al. (2016), and the dynamics of the shock detailed in the next subsection. We follow the lead of C. E. Harris et al. (2023) and R. A. Chevalier (1982) in using a volume filling factor of $f = 0.5$ for these synchrotron models. For the remainder of this paper, we will be assuming $v_{\rm wind} = 100$ km s^{-1} and a frequency $\nu = 6$ GHz for the light-curve calculations.

3.2. Shock Radius and Velocity

The evolution of the radio light curves depends on the shock dynamics (i.e., the radius and velocity). For this paper, we use the set of solutions from X. Tang & R. A. Chevalier (2017, hereafter TC17) that describes the SN blast wave as it evolves from the ejecta-dominated (ED) phase to the Sedov–Taylor (ST) phase, in contrast with our previous papers (e.g., L. Chomiuk et al. 2012b, 2016, etc.), where we assume the SN shock is ED. The relevant CSM density range for SNe Ia-CSM can be much higher than normal SNe Ia, so the swept-up CSM can be comparable to or even exceed the ejecta mass within the timescales of our observations. For example, for $\dot{M} \approx 1.0 \times 10^{-2}\, M_\odot\, {\rm yr}^{-1}$ and $v_{\rm wind} = 100\, {\rm km\, s^{-1}}$, Equation (25) in TC17 predicts that the swept-up mass will become dynamically important (i.e., $\geqslant M_{\rm ej}$) as early as 7.9 yr after explosion. At this and later times, the radius and velocity is expected to follow a ST solution, and the TC17 model accounts for this transition by smoothly connecting the ED phase to the ST phase. From these solutions, we are able to determine a shock radius and velocity for ejecta interacting with wind density profiles at late observation times.

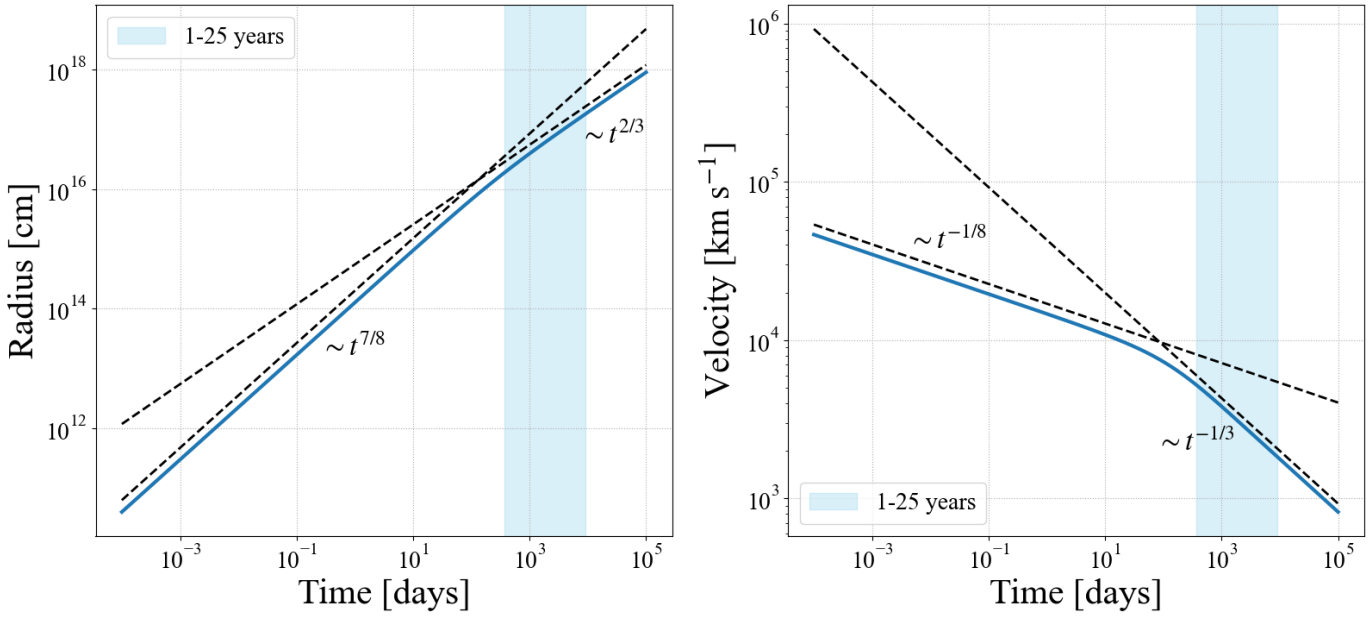

Figure 1. The time evolution of the forward shock radius (left panel) and velocity (right panel) from the TC17 model (Section 3.2) for the case of $E_{51} = 1.0$, $M_{\rm ej} = 1.44\ M_\odot$, and $\dot{M}/v_{\rm wind} = 0.1\ M_\odot\ {\rm yr}^{-1}\ (100\ {\rm km\ s}^{-1})^{-1}$. The vertical blue shaded section represents the time range at which our radio observations were obtained. Dashed lines represent the asymptotic solutions for the ED ($n = 10$ density profile) and ST cases.

For the steep ($n > 5$) ejecta profiles that are typically assumed for SNe, Equations (24) and (25) from TC17 give

$$R_s^*(t^*) = [(\zeta_s t^{*(n-3)/(n-s)})^{-\alpha} + (\xi t^{*2})^{-\alpha/(5-s)}]^{-1/\alpha}, \quad (2)$$

and

$$v_b^*(t^*) = \frac{dR_s^*}{dt^*}, \quad (3)$$

respectively. Here R_s^*, v_s^*, and t^* are dimensionless radius, velocity, and age, which are related to the physical radius (R_s), velocity (v_s), and age (t) of the shock as $R_s^* = R_s/R_{\rm ch}$, $v_s^* = v_s/v_{\rm ch}$, and $t_s^* = t/t_{\rm ch}$, where "$X_{\rm ch}$" denote the characteristic variables that are defined as

$$R_{\rm ch} = (12.9\ {\rm pc})\ M_{\rm ej}\ \dot{M}_{-5}^{-1}\ v_{\rm wind,10}, \quad (4)$$

$$t_{\rm ch} = (1.77 \times 10^3\ {\rm yr})\ E_{51}^{-1/2}\ M_{\rm ej}^{3/2}\ \dot{M}_{-5}^{-1}\ v_{\rm wind,10}, \quad (5)$$

$$v_{\rm ch} = (7.12 \times 10^3\ {\rm km\ s}^{-1})\ E_{51}^{1/2}\ M_{\rm ej}^{-1/2}, \quad (6)$$

where $M_{\rm ej}$ is the ejecta mass in terms of solar mass ($M_\odot$), and E_{51} is the kinetic energy in units of 10^{51} erg.

For a Type Ia-CSM SNe, we follow the model of an ejecta envelope with a steep density profile $n = 10$ and a wind density profile $s = 2$ (C. E. Harris et al. 2023). The values of the coefficients ζ_s, α, and ξ are drawn from Tables 4 and 6 of TC17 for an $n = 10$ ejecta profile and windlike ($s = 2$) CSM profile. The resulting solution for the dimensionless radius and velocity, after some algebraic rearrangement, is

$$R_s^*(t^*) = 1.03 t^{*(0.875)}[1 + 3.52 t^{*(0.95)}]^{-0.219}, \quad (7)$$

and

$$v_s^*(t^*) = 1.03 t^{*(-0.125)}[1 + 2.79 t^{*(0.95)}] \times [1 + 3.52 t^{*(0.95)}]^{-1.219}. \quad (8)$$

Throughout the paper, we will assume a standard SN Ia explosion with $M_{\rm ej} = 1.44\ M_\odot$ and $E_{51} = 1$.

Figure 1 illustrates the evolution of the shock radius and velocity from Equations (7) and (8). The radius follows the self-similar driven wave (or SSDW) solution (R. A. Chevalier 1982; D. K. Nadezhin 1985), with $R \propto t^{7/8}$ at early times (i.e., the ED phase), and then approaches $R \propto t^{2/3}$ for late times (i.e., the ST phase, following the self-similar ST solution; G. I. Taylor 1946; L. I. Sedov 1959). Since $v_s = dR/dt$, we see a trend of $v_s \propto t^{-1/8}$ in the ED phase, which then approaches $v \propto t^{-1/3}$ during the ST phase. The onset of the ST phase will occur earlier for denser CSM.

3.3. Basic Properties of Radio Light Curves

The radio light curves from the model described in the previous subsections are summarized in Figure 2. The shape of the light curves is similar to what has been seen in previous papers. At early times absorption processes dominate, and the radio luminosity increases in proportion to the emitting area. As the SN expands, the optical depths of the absorption processes decrease, and the light curves peak when $\tau \approx 1$, and then decline. This fading is primarily because both the energy in the electrons and the magnetic fields that are powering the emission is proportional to the shock energy ($\sim \rho v_s^2$). While the preshock density ρ decreases as r^{-2}, the shock also continues to decelerate as it loses energy to interaction with the surroundings, resulting in an overall decrease in synchrotron emission with time.

The different color lines in Figure 2 explore a sequence of $\dot{M}/v_{\rm wind}$ values. As the CSM becomes denser (i.e., higher $\dot{M}/v_{\rm wind}$), the light curves become brighter due to the increasing reservoir of shock energy (ρv_s^2) available for the amplification of magnetic fields and relativistic electrons. The duration of the free–free absorbed phase of the light curve is also longer for denser CSM (see Equation (1)), leading to the light curves peaking later in time. This is why early-time radio observations would have missed detection of SNe with denser

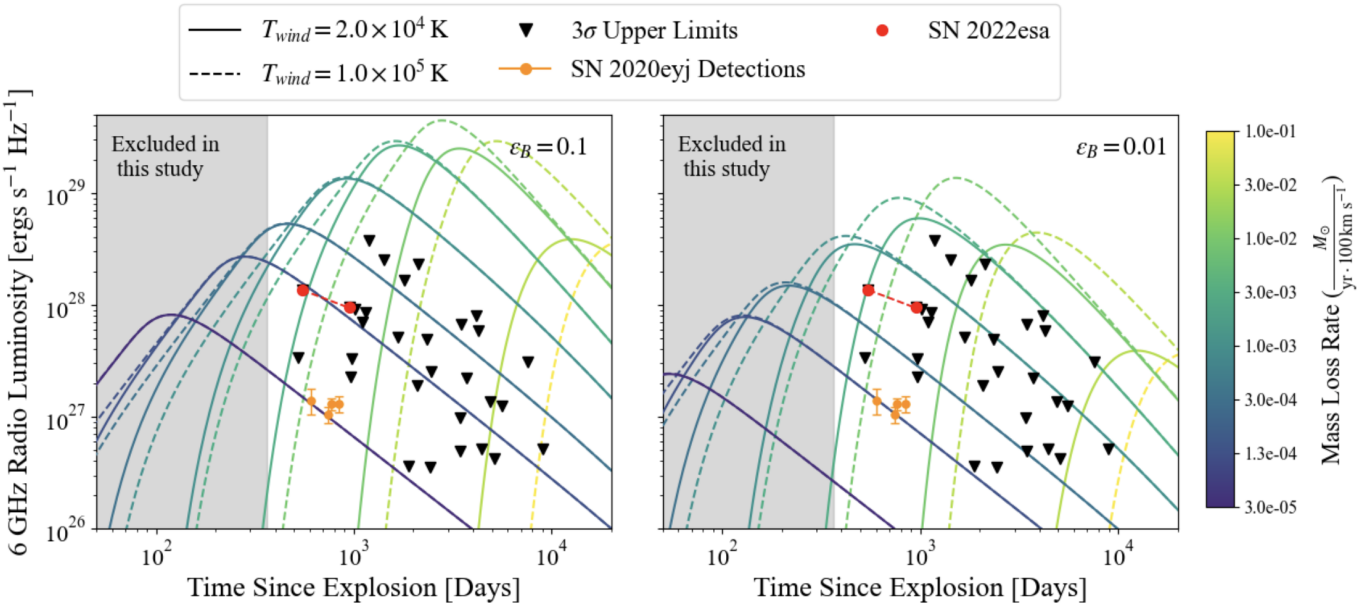

Figure 2. Predicted 6 GHz radio light curves for SNe Ia-CSM, shown alongside radio observations in this paper and from the literature. Solid curves correspond to the case of $T_{\rm wind} = 2.0 \times 10^4$ K, and dashed curves to $T_{\rm wind} = 10^5$ K. The left panel shows the case of $\epsilon_B = 0.1$, and the right panel shows $\epsilon_B = 0.01$ (both panels assume $\epsilon_e = 0.1$). Light curves span a range of $\dot{M}/v_{\rm wind}$ from $3 \times 10^{-5}\ M_\odot\ {\rm yr}^{-1}$ (dark blue lines) to $0.1\ M_\odot\ {\rm yr}^{-1}$ (yellow lines), assuming $v_{\rm wind} = 100$ km s^{-1}. The shaded gray region represents SNe Ia < 1 yr, which are excluded in this study. SNe with 3σ upper limits are plotted as inverted black triangles. The radio detections of SN 2022esa from 2023 to 2024 are shown as red circles connected by a dashed line. Literature measurements of SN 2020eyj from E. C. Kool et al. (2023) and X. Yang et al. (2023) (scaled to 6 GHz) are shown as orange points.

CSM. Above a certain mass-loss rate ($\gtrsim 5 \times 10^{-3}\ M_\odot\ {\rm yr}^{-1}$), however, the light curves begin to become fainter. This is primarily because the onset of the ST phase occurs *before* the light curve becomes optically thin (i.e., $\tau_{\rm ff} = 1$). The light curve in the ST phase declines faster because of the faster deceleration of the shock ($v \propto t^{-1/3}$). On top of this, the age at which the light curve peaks is delayed during the ST phase as the shock is evolving slower, which delays the age at which $\tau_{\rm ff} = 1$ (Equation (1)). The combination of these effects produces light curves that peak and then decline at fainter luminosities for higher mass-loss rates. This contrasts with the behavior of light curves evolving with an ED-only solution, and this is discussed further in the Appendix.

Figure 2 also illustrates the impact of the parameters ϵ_B and $T_{\rm wind}$. Lower ϵ_B means a smaller fraction of ρv_s^2 amplifies the magnetic fields, resulting in weaker fields and thus fainter luminosities. We note that the parameter ϵ_e, which we hold constant in this paper but can be uncertain, will have a similar magnitude of effect on the light curves as ϵ_B. The $T_{\rm wind}$ parameter affects the free–free optical depth $\tau_{\rm ff} \propto T_{\rm wind}^{-3/2}$ as seen in Equation (1), so hotter CSM is less opaque to synchrotron emission. We therefore see the light curves for the hotter CSM (dashed lines in Figure 2) become optically thin at earlier times. The difference between the $T_{\rm wind} = 1 \times 10^5$ K and 2×10^4 K becomes more dramatic at higher mass-loss rates, because of the effect of the ST phase described above.

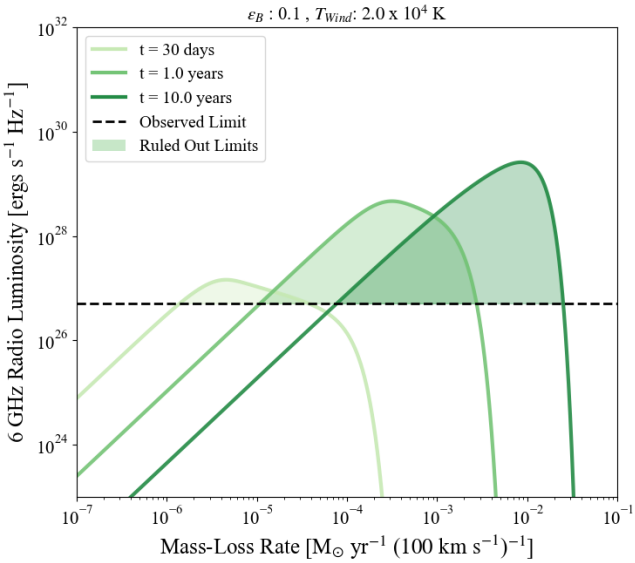

Figure 3. Illustration of how we use radio upper limits to constrain the range of *ruled-out* mass-loss rates $\dot{M}/v_{\rm wind}$ (green shade). Each light curve (green solid) shows the predicted luminosity for different mass-loss rates at a given SN age (30 days, 1 yr, and 10 yr). The range of mass-loss rates where the predicted luminosity exceeds the measured upper limit (dashed line) are ruled out. Due to the light-curve shape for windlike CSM, later-time observations are more effective at ruling out a greater (and higher) range of mass-loss rates.

3.4. Measuring Mass-loss Rates with the Light Curves

We apply the light-curve model described in Section 3.1 to the observed luminosities (or upper limits) from Table 1 to constrain the possible values of $\dot{M}/v_{\rm wind}$ for each SN using the different parameter combinations described in Table 2. In the case of a detection, we simply check for what value of $\dot{M}/v_{\rm wind}$ threads the light curve through the data point(s). For nondetections, which represent the majority of our sample, we can constrain the range of mass-loss rates ruled out by the luminosity limit as illustrated in Figure 3. At the given age of the SN, there will be a range of mass-loss rates for which the resulting luminosities at that age exceed the 3σ upper limit. These are the shaded regions in Figure 3, and represent the

Table 3
The Range of Ruled-out Mass-loss Rates for Our Ia-CSM SNe Computed with the X. Tang & R. A. Chevalier (2017) Model

SN	Model A	Model B	Model C
SN 1999E	1.8×10^{-4}–1.0×10^{-1}	1.8×10^{-4}–4.4×10^{-2}	8.7×10^{-4}–3.8×10^{-2}
SN 2002ic	4.9×10^{-4}–8.2×10^{-2}	4.9×10^{-4}–3.6×10^{-2}	3.0×10^{-3}–2.8×10^{-2}
SN 2008cg	2.0×10^{-4}–7.1×10^{-2}	2.0×10^{-4}–3.2×10^{-2}	9.4×10^{-4}–2.7×10^{-2}
SN 2009in	9.3×10^{-5}–7.0×10^{-2}	9.3×10^{-5}–3.2×10^{-2}	4.1×10^{-4}–2.8×10^{-2}
PTF10htz	1.9×10^{-4}–6.4×10^{-2}	1.9×10^{-4}–2.9×10^{-2}	8.5×10^{-4}–2.5×10^{-2}
SN 2011dz	9.2×10^{-5}–6.3×10^{-2}	9.2×10^{-5}–2.9×10^{-2}	4.0×10^{-4}–2.6×10^{-2}
SN 2011jb	4.2×10^{-4}–5.3×10^{-2}	4.2×10^{-4}–2.4×10^{-2}	2.2×10^{-3}–2.0×10^{-2}
CSS120327	5.0×10^{-4}–5.1×10^{-2}	5.0×10^{-4}–2.3×10^{-2}	2.6×10^{-3}–1.8×10^{-2}
SN 2013dn	2.0×10^{-4}–5.1×10^{-2}	2.0×10^{-4}–2.4×10^{-2}	9.0×10^{-4}–2.1×10^{-2}
SN 2014T	3.8×10^{-4}–4.5×10^{-2}	3.8×10^{-4}–2.1×10^{-2}	1.8×10^{-3}–1.7×10^{-2}
SN 2014Y	1.1×10^{-4}–5.1×10^{-2}	1.1×10^{-4}–2.3×10^{-2}	4.8×10^{-4}–2.1×10^{-2}
SN 2014ab	7.2×10^{-5}–5.3×10^{-2}	7.2×10^{-5}–2.4×10^{-2}	3.1×10^{-4}–2.2×10^{-2}
SN 2016iks	1.5×10^{-4}–3.7×10^{-2}	1.5×10^{-4}–1.7×10^{-2}	6.4×10^{-4}–1.6×10^{-2}
SN 2016jae	4.4×10^{-5}–4.1×10^{-2}	4.4×10^{-5}–1.9×10^{-2}	1.8×10^{-4}–1.8×10^{-2}
SN 2017eby	2.2×10^{-4}–3.4×10^{-2}	2.2×10^{-4}–1.6×10^{-2}	9.5×10^{-4}–1.5×10^{-2}
SN 2017ifu	5.3×10^{-4}–2.7×10^{-2}	5.3×10^{-4}–1.3×10^{-2}	2.6×10^{-3}–1.1×10^{-2}
SN 2017hzw	1.1×10^{-4}–3.3×10^{-2}	1.1×10^{-4}–1.5×10^{-2}	4.6×10^{-4}–1.5×10^{-2}
SN 2018cqj	3.6×10^{-5}–3.4×10^{-2}	3.6×10^{-5}–1.6×10^{-2}	1.5×10^{-4}–1.5×10^{-2}
SN 2018gkx	3.7×10^{-4}–2.4×10^{-2}	3.7×10^{-4}–1.1×10^{-2}	1.7×10^{-3}–1.0×10^{-2}
SN 2019agi	1.7×10^{-4}–2.6×10^{-2}	1.7×10^{-4}–1.2×10^{-2}	7.1×10^{-4}–1.2×10^{-2}
SN 2019rvb	3.9×10^{-4}–1.8×10^{-2}	3.9×10^{-4}–8.3×10^{-3}	1.8×10^{-3}–8.0×10^{-3}
SN 2020kre	4.3×10^{-4}–1.3×10^{-2}	4.3×10^{-4}–6.2×10^{-3}	2.0×10^{-3}–6.0×10^{-3}
SN 2020onv	1.6×10^{-4}–1.7×10^{-2}	1.6×10^{-4}–7.6×10^{-3}	7.0×10^{-4}–7.9×10^{-3}
SN 2020qxz	1.4×10^{-4}–1.7×10^{-2}	1.4×10^{-4}–7.5×10^{-3}	5.9×10^{-4}–7.8×10^{-3}
SN 2020abfe	1.6×10^{-4}–1.5×10^{-2}	1.6×10^{-4}–6.6×10^{-3}	6.6×10^{-4}–6.9×10^{-3}
SN 2020aeur	6.2×10^{-5}–1.7×10^{-2}	6.2×10^{-5}–7.3×10^{-3}	2.6×10^{-4}–7.7×10^{-3}
SN 2020aekp	7.9×10^{-5}–1.6×10^{-2}	7.9×10^{-5}–7.1×10^{-3}	3.3×10^{-4}–7.5×10^{-3}
SN 2022erq	4.8×10^{-5}–8.1×10^{-3}	4.8×10^{-5}–3.4×10^{-3}	2.0×10^{-4}–3.7×10^{-3}

Note. For each model from Table 2, we note the lower and upper limit of the ruled-out range in solar masses per year ($M_\odot$ yr^{-1}; 100 km s^{-1})$^{-1}$. These ranges are shown visually for each SN in Figure 4.

(This table is available in its entirety in machine-readable form in the online article.)

range of $\dot{M}/v_{\rm wind}$ that can be ruled out. The lower bound of this range comes from the optically thin (decreasing) part of the light curves, while the upper bound comes from the optically thick (rising) parts (this idea is better illustrated through the comparison of the variance in the optically thick portion of the light curves in the leftmost panel of Figure 2 to the upper limits derived for Models A and B in Table 3). The range will additionally depend on the assumed values of ϵ_B and $T_{\rm wind}$, and we discuss this further in Section 4.

Figure 3 also nicely illustrates the benefit of obtaining late-time observations for our sample. For the same upper limit, observations at 30 days would have only ruled out an order-of-magnitude range of possible mass-loss rates, while at 10 yr more than a 2 orders-of-magnitude range is ruled out, shifted to the *higher* values of $\dot{M}/v_{\rm wind}$ that are more relevant for SNe Ia-CSM. This is again due to the free–free absorption described in the previous section, which suppresses the radio emission from SNe for longer periods at higher mass-loss rates.

4. Results

Most of the SNe (28 out of 29) in our sample are nondetections at 6 GHz, and their 3σ upper limits are shown in Figure 2. Based on the synchrotron emission model in Section 3, these upper limits rule out a range of mass-loss rates for each SN, shown in Figure 4, with the specific ranges for each SN reported in Table 3.

We find that the radio upper limits rule out the mass-loss rate range between $\sim10^{-4}$ and 10^{-2} $M_\odot$ yr^{-1} (assuming v_w = 100 km s^{-1}) for most of our sample, with the exact ruled-out range varying with the SN age when the radio observation was carried out, as well as the assumed values of ϵ_B and $T_{\rm wind}$. For example, decreasing ϵ_B by 1 dex (i.e., from 0.1 to 0.01) yields an increase of 0.68 dex in the $\dot{M}$ lower limits and a decrease of 0.05 dex in the upper limits, on average. The variation of $T_{\rm wind}$ has more of an effect on the upper limits of $\dot{M}$, while there is a negligible effect on the lower limits when retaining the same value for ϵ_B. For instance, when $\epsilon_B = 0.1$ stays the same and $T_{\rm wind}$ increases by 0.7 dex (from 2.0×10^4 K to 1.0×10^5 K), the change in the lower limits is negligible while the upper limits increase by an average of 0.35 dex. Lowering the value of ϵ_B for the same $T_{\rm wind}$ pushes down the light curve to fainter luminosities, which makes the lower limit of the ruled-out mass-loss rates less constraining.

The range of excluded mass-loss rates progressively shifts higher for older SNe in Figure 4. For instance, we see that our radio observations of SN 2022erq rule out $2.0 \times 10^{-4} < \dot{M} < 3.7 \times 10^{-3}$ $M_\odot$ yr^{-1}, for $\epsilon_{\rm B} = 0.01$, $T_{\rm wind} = 2 \times 10^4$ K, and $v_{\rm wind} = 100$ km s^{-1}, whereas we exclude $8.7 \times 10^{-4} < \dot{M} < 3.8 \times 10^{-2}$ $M_\odot$ yr^{-1} for SN 1999E for the same values of ϵ_B, $T_{\rm wind}$, and $v_{\rm wind}$ (exact values are recorded in Table 3). This is

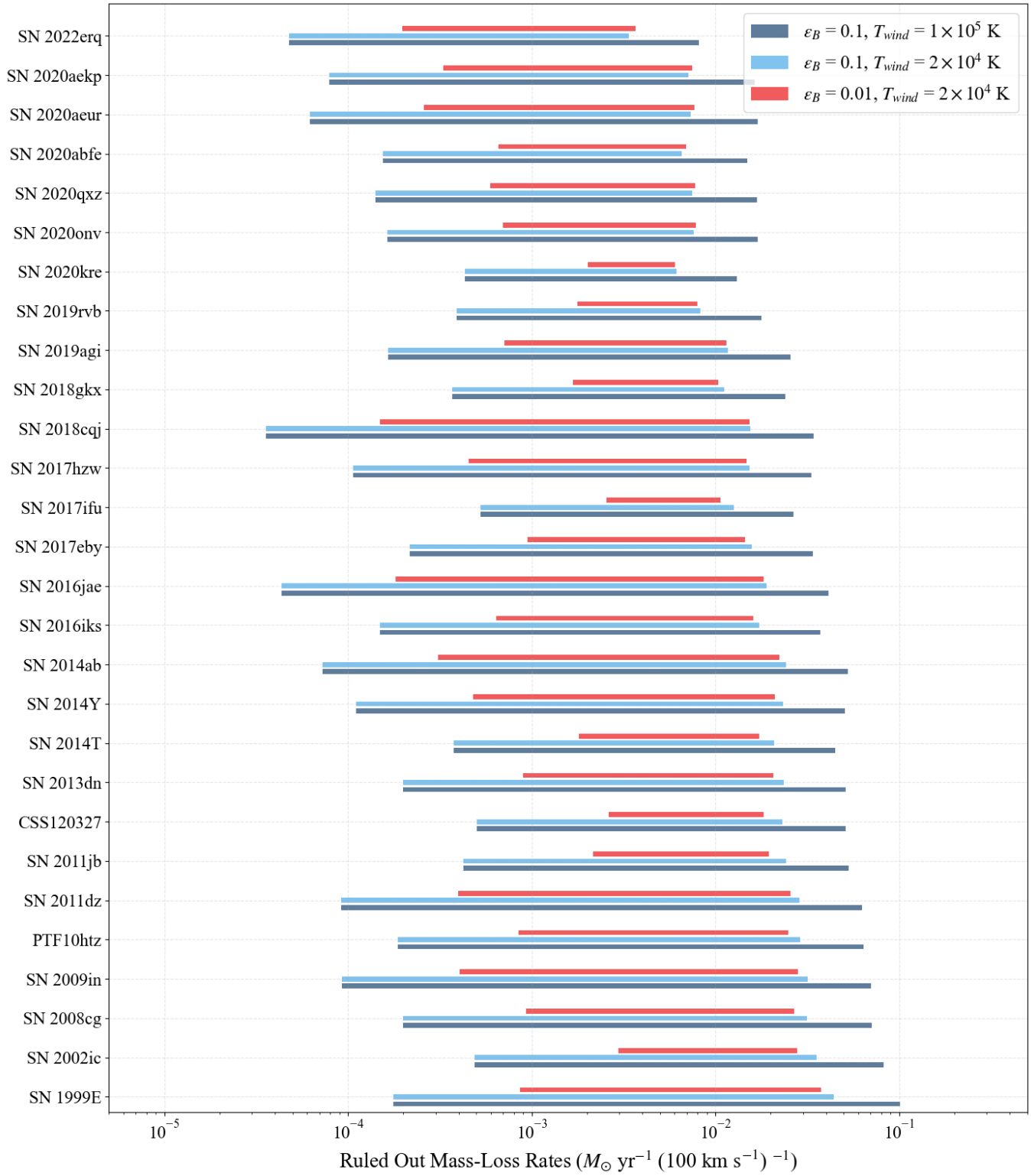

Figure 4. The range of mass-loss rates ruled out by the radio upper limits for each SN. For each SN, we show ranges for the three models in Table 2 for the parameters ϵ_B and $T_{\rm wind}$. See Section 4 for details.

because of the effect observed in Figure 3 and discussed in Section 3.4, where at older ages the SN observations are more sensitive to emission from higher mass-loss rates that emerge progressively later in time. This effect is additionally observed in Figure 6, particularly in the behavior of the light curves evolving with an ED-only solution. The progression in Figure 7 is however non-monotonic, as some SNe are more distant than others, thus having shallower limits (e.g., the ruled-out range of SN 2019agi is significantly smaller than the range for SN 2018cqj, even though they are a year apart, because SN 2018cqj is nearly 3 times closer).

We briefly discuss SN 2022esa, the only SN radio-detected SN our sample. While it was initially classified as a SN Ia-CSM,[14] reinspection of the public TNS spectrum shows that the narrow lines are likely from the host galaxy, given the visible [O III] and [S II] lines in addition to the narrow Balmer lines. Removing these lines using `SNID emclip` (S. Blondin & J. L. Tonry 2007) does not provide a very reliable classification. In addition, a subsequent spectrum obtained at the Nordic Optical Telescope on 2022 July 17 show better matches with a stripped-envelope core-collapse SN (Type Ib/c), and late nebular spectra reveal lines of oxygen and carbon but no lines from Fe-peak elements (Y. Qin 2025, private communication), which further argues for a core-collapse origin (Y. Qin et al. 2025, in preparation). A more detailed investigation of the object will be presented in Qin et al. (2025, in preparation), but here we briefly note the radio evolution observed for 2022esa. Figure 6 shows the observed VLA measurements, showing a clear decline in radio emission similar to SN 2020eyj, except that it is much brighter. The slope of the decline is slightly shallower than our ST phase light curves. The mass-loss rates that best fit these data points are in the range of $(1.2 - 1.5) \times 10^{-4}\ M_\odot\ \mathrm{yr}^{-1}$ ($\epsilon_B = 0.1$) or $(5 - 6.4) \times 10^{-4}\ M_\odot\ \mathrm{yr}^{-1}$ ($\epsilon_B = 0.01$).

We also reinterpret the radio data for SN 2020eyj, which is still the only radio-detected Ia-CSM, with the modified radio light-curve model in this paper. SN 2020eyj was observed at 5.1 GHz with e-MERLIN in E. C. Kool et al. (2023) on 2021 November 19, then again during six consecutive days between 2022 April 6–12. This SN was also observed with the VLA in X. Yang et al. (2023) on both 2022 April 14 and June 26. The data collected from these e-MERLIN and VLA observations are shown as orange points in Figure 2. SN 2020eyj was consistent with constant or slightly decreasing flux over these radio observations, meaning we can assume the emission is optically thin. We scale the e-MERLIN measurements to 6 GHz assuming the luminosity $L_\nu \propto \nu^{-1}$. We find that the luminosities are consistent with mass-loss rates of $3.4 \times 10^{-5}\ M_\odot\ \mathrm{yr}^{-1}$ for $\epsilon_B = 0.1$ and $1.4 \times 10^{-4}\ M_\odot\ \mathrm{yr}^{-1}$ for $\epsilon_B = 0.01$. The assumed value of $T_{\rm wind}$ should not affect the mass-loss rates, as the emission is optically thin. Our measurements are lower than in E. C. Kool et al. (2023) because of their lower fitted values of ϵ_B, which we return to in Section 5.

5. Discussion

Our results indicate that the majority of SNe Ia-CSM do not produce luminous radio emission at 6 GHz on ∼1–25 yr timescales, in contrast with SN 2020eyj.[15] The nondetections of our sample also stand in contrast with Type IIn SNe, the core-collapse cousins of SNe Ia-CSM, where at least 10% of the population with radio observations have detectable light curves that peak on timescales of about 2–34 yr (substantially longer than other core-collapse SN subtypes) at luminosities comparable to our upper limits (see P. Chandra 2018; M. F. Bietenholz et al. 2021, and references therein). One possibility is that, assuming both types of SNe explode with the canonical 10^{51} erg energy, the Ia-CSM SNe on average have lower CSM densities than Type IIn SNe, and thus the radio-detectable Ia-CSM population may be peaking at times similar to SN 2020eyj, i.e., a year or two after explosion (as opposed to longer few-decade timescales like SNe IIn). A similar reasoning was applied to X-ray observations of SNe Ia-CSM, where it was argued that SN 2012ca remains the only X-ray-detected SN Ia because it was likely observed at an opportune moment when the ambient medium was dense enough to produce visible X-rays but not too dense to suffer complete absorption (C. D. Bochenek et al. 2018; V. V. Dwarkadas 2023, 2024). In this paper, we present only two SNe with radio observations at $\lesssim$2 yr ages: SN 2022erq, which was a nondetection, and SN 2022esa, which was likely a peculiar Ic. L. Chomiuk et al. (2016) compiles radio upper limits for six more SNe Ia-CSM in the first year of explosion. These observations imply that luminous radio emission in the first 1–2 yr is also unlikely to be common, but more sensitive constraints and larger samples can further test this hypothesis in the future.

The range of mass-loss rates ruled out by our radio survey, roughly between 10^{-4} and $10^{-2}\ M_\odot\ \mathrm{yr}^{-1}$, is somewhat in tension with the mass-loss rates derived from optical observations of SNe Ia-CSM. These rates are most commonly derived by modeling the broad component of the Hα line as $L_{\rm H\alpha} = \frac{1}{4}\,\epsilon_{\rm Ha}(\dot{M}/v_{\rm wind})v_s^3$, assuming hydrogen in a spherically symmetric CSM with a r^{-2} profile is being collisionally excited by the shock (e.g., N. N. Chugai 1991; I. Salamanca et al. 1998). The observed luminosities and velocities of ∼a few $\times\ 10^3$ km s^{-1}, measured from the broad Hα line profiles in the first ∼year following explosion, yield mass-loss rates typically in the range of 10^{-4}–$10^{-2}\ M_\odot\ \mathrm{yr}^{-1}$, assuming 100 km s^{-1} winds and an efficiency $\epsilon_{\rm H\alpha} = 0.1$ (e.g., G. Aldering et al. 2006; J. M. Silverman et al. 2013; Y. Sharma et al. 2023). This range of mass-loss rates is generally inconsistent with our radio-derived constraints on $\dot{M}$ in Figure 4 for the same CSM geometry. Based on the radio measurements alone, the required mass-loss rates would have to be lower than $10^{-4}\ M_\odot\ \mathrm{yr}^{-1}$ or higher than 10^{-2}–$10^{-1}\ M_\odot\ \mathrm{yr}^{-1}$. However, we point out the radio observations presented here, obtained years after explosion, probe the CSM at significantly larger radii than the Hα measurements. Specifically, optical Hα implies mass-loss rates of $\sim 10^{-4}$–$10^{-2}\ M_\odot\ \mathrm{yr}^{-1}$ at $R_{\rm in} = 10^{15}$–10^{16} cm, while our radio limits apply to radii in the range of 10^{17}–10^{18} cm. Radio observations of several SNe Ia-CSM do exist in epochs overlapping Hα measurements, but these also yield nondetections (L. Chomiuk et al. 2016). In fact, these nondetections from earlier-time (<1 yr) radio observations push the lower end of the ruled-out $\dot{M}$ range further down to $\lesssim 10^{-5.5}\ M_\odot\ \mathrm{yr}^{-1}\ (100\ \mathrm{km\ s^{-1}})^{-1}$ (e.g., B. Dilday et al. 2012; L. Chomiuk et al. 2016). While such low mass-loss rates are more consistent with realistic progenitors like symbiotic binaries (E. R. Seaquist & A. R. Taylor 1990; L. Chomiuk et al. 2012b), they may underpredict the Hα luminosities, requiring a substantially more efficient $\epsilon_{\rm Ha}$ or faster shock velocities than measured from the broadened Hα.

Mass-loss rates higher than $0.1\ M_\odot\ \mathrm{yr}^{-1}(100\ \mathrm{km\ s^{-1}})^{-1}$ are also allowed by the radio limits, and we do note that mass-loss rates derived from modeling the bolometric light curves of SNe Ia-CSM in J. M. Silverman et al. (2013) are $\gtrsim 10^{-1}\ M_\odot\ \mathrm{yr}^{-1}$. However, these high values are more inconsistent with windlike CSM in single-degenerate systems. In fact, such copious winds are extreme even for typical supergiant stars, and only observed in luminous blue variable eruptions (N. Smith 2014).

[14] TNS classification (https://www.wis-tns.org/object/2022esa/classification-cert).

[15] We also note that 2020eyj was a He-rich Ia-CSM (E. C. Kool et al. 2023), which contrasts with our sample that are H-rich Ia-CSM.

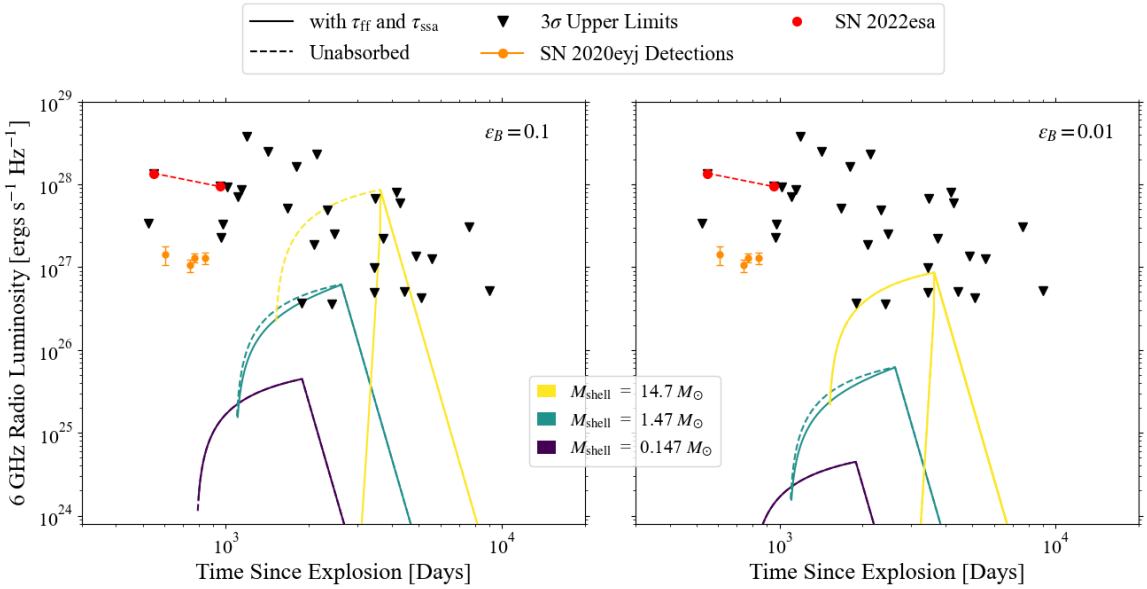

Figure 5. 6 GHz light curves produced by interaction with shell-like CSM, compared with our radio observations of SNe Ia-CSM. The light curves accounting for absorption are solid, whereas the ones with no absorption are dashed. The left panel shows models for $\epsilon_B = 0.1$, and the right panel for $\epsilon_B = 0.01$ (both panels use $\epsilon_e = 0.1$). Each light curve's color is specific to the density and mass of the shell, with the dark purple color representing $\rho_{csm} = 10^{-20}$ g cm^{-3} and $M_{shell} = 0.147$ $M_\odot$, teal corresponding to $\rho_{csm} = 10^{-19}$ g cm^{-3} and $M_{shell} = 1.47$ $M_\odot$, and yellow depicting $\rho_{csm} = 10^{-18}$ g cm^{-3} and $M_{shell} = 14.7$ $M_\odot$. We assume $R_{in} = 10^{17}$ cm and $f_R = 1$ for this model (see Section 5).

A possible way to reconcile the tension between radio and optical observations of SNe Ia-CSM is if the microparameters ϵ_B and ϵ_e are significantly lower than the range assumed here (10^{-2}–10^{-1}). Lowering these parameters makes the radio luminosities fainter (as discussed in Section 3.3), which shrinks the range of ruled-out mass-loss rates further (Figure 4). For $\epsilon_B < 10^{-4}$, the light curves for the majority of our sample fall below our observed limits, and no mass-loss rate can be ruled out. E. C. Kool et al. (2023) showed that the bolometric light curve of SN 2020eyj suggested wind mass-loss rates of 10^{-4} to 3×10^{-3} $M_\odot$ yr^{-1} for $v_{wind} = 100$ km s^{-1}, which could fit the radio observations only if $\epsilon_B = 1.7 \times 10^{-3}$ or 1.5×10^{-5}. On the other hand, $\epsilon_B = 0.1$ was consistent with the radio light curve of SN 2020eyj for a shell-like CSM geometry like in C. E. Harris et al. (2016; Figure 4 in E. C. Kool et al. 2023). Unfortunately, the observational and theoretical basis for determining values of ϵ_e and ϵ_B is still a topic of debate. Values of ϵ_B =0.01–0.1 have been inferred in relativistic SNe (e.g., R. A. Chevalier & C. Fransson 2006; A. M. Soderberg et al. 2012), and given the similar polytropic structure of their progenitors and white dwarfs, this range has been conventionally assumed for SNe Ia (L. Chomiuk et al. 2012b). Values of ϵ_e and $\epsilon_B \gtrsim 10^{-3}$ have been inferred in shocks with velocities of a few $\times$ 10^3 km s^{-1} in the Kepler SN remnant (S. P. Reynolds et al. 2021), also a candidate for a Type Ia that exploded in a dense CSM (e.g., S. Katsuda et al. 2015). Similar values were also derived from radio light curves of some Type II SNe (R. A. Chevalier et al. 2006). Theoretically, a clear prescription of how these parameters change with the shock conditions and shock structure in collisionless shocks is also yet to be established (see review in A. Marcowith et al. 2016), so we do not have firm evidence leading us to prefer lower values of ϵ_B.

Another possible way of addressing the tension is if the CSM is not distributed as a wind, but rather discrete, dense shells produced by episodic mass-loss events such as common-envelope ejections (e.g., M. Livio & A. G. Riess 2003) or swept-up nova shells (e.g., W. M. Wood-Vasey & J. L. Sokoloski 2006; K. Moore & L. Bildsten 2012). Such shell-like geometries, with thicknesses of up to 4 times the inner radii, have been proposed in some SNe Ia showing delayed interactions, like PTF11kx and SN 2002ic (e.g., B. Dilday et al. 2012; M. L. Graham et al. 2017; C. E. Harris et al. 2018). This shock+shell interaction beginning a few months after explosion would power Hα, but then rapidly diminish once the shock crosses over the shell, eluding later radio observations. In fact, radio observations of SN 2020eyj were reproduced with a best-fit shell $\sim$0.3 $M_\odot$ located within 10^{17} cm, but the resulting luminosity is expected to diminish well below 10^{27} erg s^{-1} Hz^{-1} (the lower end of our limits in Figure 2) by 10^3 days according to Figure 4 in E. C. Kool et al. (2023).

We consider the models of SN interaction with shell-like CSM from C. E. Harris et al. (2016, 2021), where a shell is characterized by a constant mass density ρ_{csm}, an inner radius R_{in}, and a width of the shell (f_R, which is described as a fraction of R_{in}). Because shells are characterized by more parameters than windlike CSM, detailed constraints on shell-like CSM are outside the scope of this paper. However, to give a sense of what sorts of shells can be constrained by current observations, Figure 5 shows a few example light curves for shells spanning 2 orders of magnitude in mass. Models assuming $\epsilon_B = 0.1$ are shown in the left panel and $\epsilon_B = 0.01$ in the right panel; in both panels, we take $\epsilon_e = 0.1$ and assume a temperature of the shell (which is assumed to be ionized) of 2×10^4 K. The models shown take $R_{in} = 10^{17}$ cm to yield interaction around the time of our observational constraints (smaller R_{in} leads to earlier radio emission), and assume $f_R = 1$ (thicker shells lead to longer-lasting radio emission). The unabsorbed light curves are plotted as dashed lines, and rise

rapidly after the start of interaction with the shell, and plummet once the shock traverses the shell. The unabsorbed peak spectral radio luminosity (in erg s^{-1} Hz^{-1}) is $L_\nu = 1.7 \times 10^{54}\ \epsilon_e^2\ \epsilon_B\ \nu^{-1}\ \rho_{\rm csm}^{8/7}\ r_{\rm in}^{3/7}\ (1-(1+f_r)^{-1.28})$. Using the expressions of C. E. Harris et al. (2021), we correct the radio light curves for both synchrotron self-absorption and free–free absorption, and plot these as solid lines. In the case of the densest shell ($\rho_{\rm csm} = 10^{-18}$ g cm^{-3}, $M_{\rm shell} =$ 14.7 $M_\odot$), absorption strongly affects the light curve, narrowing it to a brief burst emitted when the shock reaches the outer edge of the shell. The 1.47 $M_\odot$ shell model is barely affected by absorption, and the 0.147 $M_\odot$ shell model not at all.

Figure 5 demonstrates that for a shell to be detectable by our radio observations of SNe Ia-CSM, it needs to be quite dense and massive. The lower-mass shells of $\sim$0.1 $M_\odot$ (which might be expected from a shell produced by several recurrences of a nova) are not expected to be detectable at radio wavelengths at these distances. Our most sensitive limits can constrain shells of $\sim$1 $M_\odot$ (as might be expected from a common-envelope ejection event). Our less sensitive limits require densities/masses an order of magnitude higher. At these higher densities, absorption is important, narrowing the light curve and requiring an observer to get very lucky to capture the transient radio signal.

And yet, the observations of SNe Ia-CSM presented here still have potential to rule out common envelopes surrounding the explosion. A significant fraction of planetary nebulae are the result of common-envelope ejection, and systems like the Ring Nebula and NGC 6818 show densities of several $\times$ 10^2–10^3 cm^{-3} over radii spanning 10^{16} cm to several $\times$ 10^{17} cm (S. Benetti et al. 2003; C. R. O'Dell et al. 2007). These shells are so radially extended that they are not well modeled by the equations of C. E. Harris et al. (2016, 2021), which are calibrated for $f_R = 0.1$–1, and they might be better approximated with a uniform medium. Interaction with a uniform medium of density 10^3 cm^{-3} yields a detectable radio luminosity, 3×10^{27} erg s^{-1} Hz^{-1} on day 1000 for $\epsilon_B = 0.1$ (and becomes more luminous with time; L. Chomiuk et al. 2016). While more work is needed to predict the radio light curves expected from interaction with a planetary-nebula-like CSM (especially when accounting for likely departures from spherical symmetry), this back-of-the-envelope estimate implies they are likely detectable around SNe Ia-CSM with current radio telescopes. The assumption of spherical steady mass loss is likely violated in most progenitors, but the limits we estimate in this paper still exclude average mass-loss densities in the ruled-out range.

6. Conclusions

Motivated by the recent (and first ever) radio detection of SN Ia-CSM SN 2020eyj at $\sim$1.5–2 yr, we have carried out the largest late-time (>1 yr) radio survey of SNe Ia-CSM to date. The goal was to detect synchrotron emission from shock interaction with a high-density CSM, as suggested by optical observations, that would have eluded earlier observations due to heavy synchrotron and free–free absorption.

We observed 29 historical SNe Ia-CSM with ages of 1–25 yr with the VLA for about 10–20 minutes each, deep enough to detect emission at levels similar to SN 2020eyj. Images were calibrated and reconstructed with standard pipelines, and the flux densities (or upper limits) at the SN locations were analyzed with standard synchrotron emission models from SN shocks interacting with r^{-2}-like CSM wind. We used a new model of the shock dynamics from TC17 that includes a ST evolution of the shock if the swept-up CSM mass becomes comparable to or exceeds the ejecta mass. The new light-curve model predicts increasingly fainter emission at higher mass-loss rates as a result of the enhanced deceleration of the forward shock.

Most of our SNe (28 out of 29) are radio nondetections down to 3σ limits of $\lesssim$35 μJy, implying that emergent radio emission (similar to SN 2020eyj) at these brightness levels on 1.5–25 yr timescales is unlikely in SNe Ia-CSM. The only radio-detected object in the sample, SN 2022esa, is most likely a peculiar SN Ic based on inspection of spectra taken at later epochs. Nevertheless, we have compiled the *largest* sample of SNe Ia-CSM with radio upper limits in this paper, which allows us for the first time to independently verify the mass-loss rates of SNe Ia-CSM quoted from optical observations. We find that the radio upper limits of our sample rule out mass-loss rates between $\sim 10^{-4}$ and 10^{-2} $M_\odot$ yr^{-1} (100 km s^{-1})$^{-1}$ (though the range differs for each SN and assumed model parameter). This is inconsistent with the mass-loss rates predicted by models of the Hα line, yet consistent with the high mass-loss rates ($>10^{-1}$ $M_\odot$ yr^{-1}) derived from bolometric light-curve models of SNe Ia-CSM. We believe the best way to reconcile radio and optical constraints is either that the CSM has more complex, discontinuous geometries than a wind (e.g., shells that only produce transient Hα/radio emission), or that the CSM can be a wind, but the efficiency parameters of accelerating electrons (ϵ_e) and amplifying magnetic fields (ϵ_B) are much smaller for SNe Ia-CSM ($<10^{-4}$–10^{-3}) than generally assumed for SNe Ia.

We hope the dataset presented here will be a valuable resource to the community for additional investigations of SNe Ia-CSM. We particularly encourage coordinated optical and radio observations to better constrain CSM with discontinuous, shell-like geometries. The upcoming Rubin observatory, as well as high-sensitivity all-sky radio surveys with DSA-2000 (G. Hallinan et al. 2019), the Square Kilometre Array (P. E. Dewdney et al. 2009), and ngVLA (E. J. Murphy et al. 2018), will not only enable such coordinated observations but also reach greater sensitivities than our current observations.

Acknowledgments

O.G., G.S., C.E.H., and L.C. are grateful for support from NSF grants AST-2107070 and AST-2205628. J.M. and M.P.T. acknowledge financial support through the Severo Ochoa grant CEX2021-001131-S and the Spanish National grant PID2023-147883NB-C21, funded by MCIU/AEI/10.13039/501100011033, as well as support through ERDF/EU. The National Radio Astronomy Observatory is a facility of the National Science Foundation operated under cooperative agreement by Associated Universities, Inc.

Facility: VLA.

Software: `CASA` (J. P. McMullin et al. 2007), `astropy` (Astropy Collaboration et al. 2022), `matplotlib` (J. D. Hunter 2007), `scipy` (P. Virtanen et al. 2020), `numpy` (C. R. Harris et al. 2020), `photutils` (L. Bradley et al. 2023).

Appendix
Comparison of X. Tang & R. A. Chevalier (2017) with Previous Models

Here we discuss the difference between the light curves based on the shock dynamics of the TC17 model that includes both ED and ST evolution, and those assumed in previous radio studies of SNe Ia (e.g., L. Chomiuk et al. 2016) that only included the ED solution, $R \propto t^{(n-3)/(n-s)}$. For our assumed $n = 10$ ejecta and windlike CSM ($s = 2$), the ED solution implies $R_s \propto t^{7/8}$ and $v_s \propto t^{-1/8}$. While the ED solution is applicable to the general SN Ia population where CSM densities are expected to be low (L. Chomiuk et al. 2016), it can lead to very different light curves at high CSM densities compared to those including the ST phase.

This effect is illustrated in Figure 6, where we plot the ED +Sedov-based light curve (the "TC17 model") in solid, and the ED-only light curves from previous models (the "Old Model") in dashed. For lower mass-loss rates ($<10^{-4}\ M_\odot\ \mathrm{yr}^{-1}$), the light curves for the two models are almost identical since the shock is ED in both models; the Sedov phase has not set in during the timescale of our observations. At higher mass-loss rates, the difference between the two models become more dramatic, with the TC17 model showing decreasing luminosities with increasing mass-loss rate, while the old models show increasing luminosities. The difference, as mentioned in Section 3.3, is because at high densities the onset of the Sedov phase is occurring before the light curve becomes optically thin to free–free absorption. The Sedov solution has a higher rate of deceleration than the ED phase, so the decrease in the magnetic field and electron energy densities (that power the synchrotron emission) is occurring faster. By the time the light curve emerges from free–free absorption, therefore, the luminosity has already significantly decreased compared to the ED case, giving an overall fainter light curve in the TC17 models.

In Figure 7, we see the difference between the two models in the range of mass-loss rates ruled out by observations. The difference in the lower end of the ruled-out range between the two models is minor (∼0.1 dex, the largest being 0.4 dex in SN 2002ic for $\epsilon_B = 0.01$, $T_{\rm wind} = 2 \times 10^4$ K), caused mainly by the slightly steeper slope of the light curve in the ST phase for mass-loss rates approaching $10^{-3}\ M_\odot\ \mathrm{yr}^{-1}$ $(100\ \mathrm{km\ s}^{-1})^{-1}$. We see a more noticeable difference between the two models for the upper end of the ruled-out range (with TC17 on average being 0.4 dex lower, the largest being 0.7 dex in SN 1999E). This difference gets larger for older SNe because the light curves of the "Old Model" get brighter with mass-loss rate, and so a larger extent (in mass-loss rate) of the light curve can be excluded by the upper limit (Figure 3). Additionally, the time when $\tau_{\rm ff} \gtrsim 1$ is prolonged for the TC17 model because of the slower evolution of the shock, further restricting the upper limit that can be constrained.

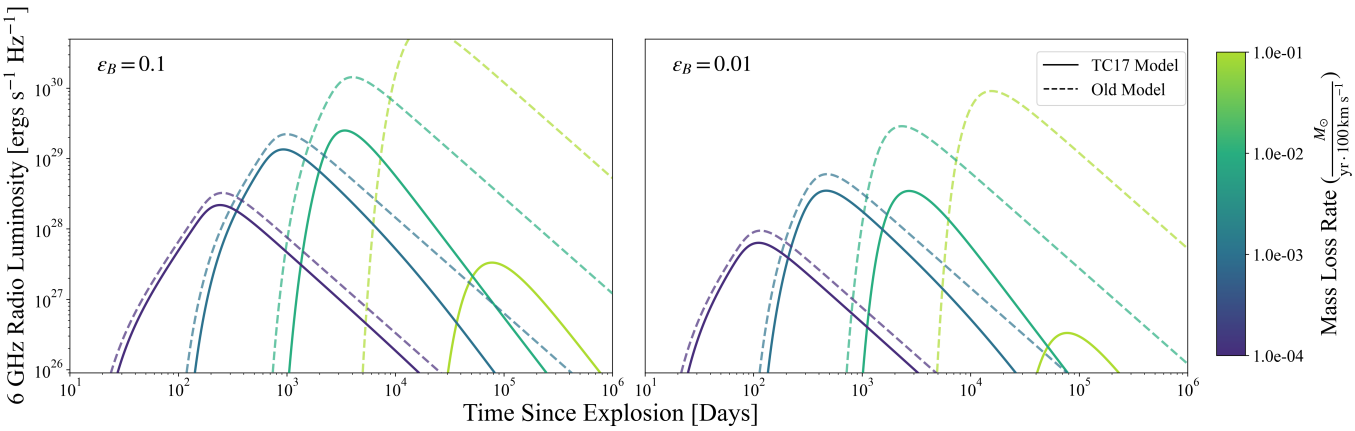

Figure 6. Comparison of light curves produced by the different models. The solid lines make use of the dynamics from TC17, while the dashed lines represent the models of L. Chomiuk et al. (2016), which do not include the transition to the ST phase. The left panel shows models for $\epsilon_B = 0.1$, and the right panel for $\epsilon_B = 0.01$. Different color lines represent different values of $\dot{M}/v_{\rm wind}$, according to the color bar at right.

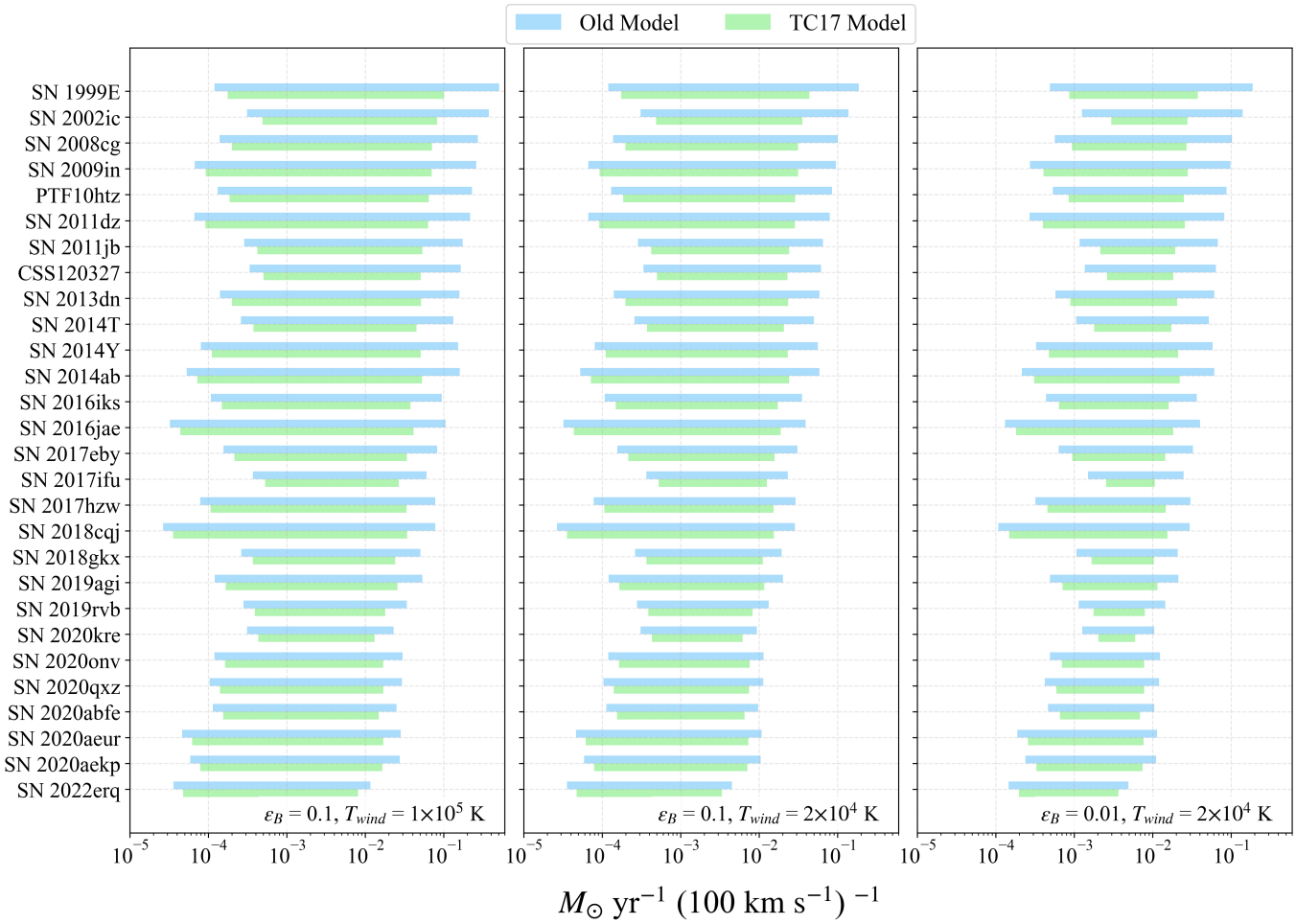

Figure 7. Comparing the TC17 model (green) with the older, ED light-curve models (blue). Each panel represents the parameter value combinations from Table 2. See the Appendix for details. This figure does not include data for SN 2022esa.

ORCID iDs

Olivia Griffith https://orcid.org/0009-0000-2643-4753
Grace Showerman https://orcid.org/0009-0000-2871-9330
Sumit K. Sarbadhicary https://orcid.org/0000-0002-4781-7291
Chelsea E. Harris https://orcid.org/0000-0002-1751-7474
Laura Chomiuk https://orcid.org/0000-0002-8400-3705
Jesper Sollerman https://orcid.org/0000-0003-1546-6615
Peter Lundqvist https://orcid.org/0000-0002-3664-8082
Javier Moldón https://orcid.org/0000-0002-8079-7608
Miguel Pérez- Torres https://orcid.org/0000-0001-5654-0266
Erik C. Kool https://orcid.org/0000-0002-7252-3877
Takashi J. Moriya https://orcid.org/0000-0003-1169-1954

References

Aldering, G., Antilogus, P., Bailey, S., et al. 2006, ApJ, 650, 510
Astropy Collaboration, Price-Whelan, A. M., Lim, P. L., et al. 2022, ApJ, 935, 167
Benetti, S., Cappellaro, E., Ragazzoni, R., Sabbadin, F., & Turatto, M. 2003, A&A, 400, 161
Bietenholz, M. F., Bartel, N., Argo, M., et al. 2021, ApJ, 908, 75
Blondin, S., & Tonry, J. L. 2007, ApJ, 666, 1024
Bochenek, C. D., Dwarkadas, V. V., Silverman, J. M., et al. 2018, MNRAS, 473, 336
Bradley, L., Sipőcz, B., Robitaille, T., et al. 2023, Astropy/Photutils: v1.9.0, Zenodo, doi:10.5281/zenodo.8248020
Burns, C. R., Parent, E., Phillips, M. M., et al. 2018, ApJ, 869, 56
CASA Team, Bean, B., Bhatnagar, S., et al. 2022, PASP, 134, 114501
Chandra, P. 2018, SSRv, 214, 27
Chevalier, R. A. 1982, ApJ, 258, 790
Chevalier, R. A. 1998, ApJ, 499, 810
Chevalier, R. A., & Fransson, C. 2006, ApJ, 651, 381
Chevalier, R. A., & Fransson, C. 2017, Handbook of Supernovae (Springer), 875
Chevalier, R. A., Fransson, C., & Nymark, T. K. 2006, ApJ, 641, 1029
Chomiuk, L., Krauss, M. I., Rupen, M. P., et al. 2012a, ApJ, 761, 173
Chomiuk, L., Soderberg, A. M., Chevalier, R. A., et al. 2016, ApJ, 821, 119
Chomiuk, L., Soderberg, A. M., Moe, M., et al. 2012b, ApJ, 750, 164
Chomiuk, L., & Wilcots, E. M. 2009, ApJ, 703, 370
Chugai, N. N. 1991, MNRAS, 250, 513
Darnley, M. J., Hounsell, R., O'Brien, T. J., et al. 2019, Natur, 565, 460
Dewdney, P. E., Hall, P. J., Schilizzi, R. T., & Lazio, T. J. L. W. 2009, IEEEP, 97, 1482
Dilday, B., Howell, D. A., Cenko, S. B., et al. 2012, Sci, 337, 942
Dwarkadas, V. V. 2023, MNRAS, 520, 1362
Dwarkadas, V. V. 2024, MNRAS, 533, 27
Fox, O. D., Silverman, J. M., Filippenko, A. V., et al. 2015, MNRAS, 447, 772
Fransson, C., Lundqvist, P., & Chevalier, R. A. 1996, ApJ, 461, 993
Graham, M. L., Harris, C. E., Fox, O. D., et al. 2017, ApJ, 843, 102
Graham, M. L., Harris, C. E., Nugent, P. E., et al. 2019, ApJ, 871, 62
Hallinan, G., Ravi, V., Weinreb, S., et al. 2019, BAAS, 51, 255, https://ui.adsabs.harvard.edu/abs/2019BAAS...51g.255H/abstract
Hamuy, M., Phillips, M. M., Suntzeff, N. B., et al. 2003, Natur, 424, 651
Han, Z., & Podsiadlowski, P. 2006, MNRAS, 368, 1095

Harris, C. E., Chomiuk, L., & Nugent, P. E. 2021, ApJ, 912, 23
Harris, C. R., Millman, K. J., van der Walt, S. J., et al. 2020, Natur, 585, 357
Harris, C. E., Nugent, P. E., Horesh, A., et al. 2018, ApJ, 868, 21
Harris, C. E., Nugent, P. E., & Kasen, D. N. 2016, ApJ, 823, 100
Horesh, A., Kulkarni, S. R., Fox, D. B., et al. 2012, ApJ, 746, 21
Harris, C. E., Sarbadhicary, S. K., Chomiuk, L., et al. 2023, ApJ, 952, 24
Hosseinzadeh, G., Sand, D. J., Sarbadhicary, S. K., et al. 2023, ApJL, 953, L15
Hunter, J. D. 2007, CSE, 9, 90
Iben, I., & Tutukov, A. V. 1984, ApJS, 54, 335
Inserra, C., Fraser, M., Smartt, S. J., et al. 2016, MNRAS, 459, 2721
Jha, S. W., Maguire, K., & Sullivan, M. 2019, NatAs, 3, 706
Katsuda, S., Mori, K., Maeda, K., et al. 2015, ApJ, 808, 49
Kool, E. C., Johansson, J., Sollerman, J., et al. 2023, Natur, 617, 477
Leloudas, G., Hsiao, E. Y., Johansson, J., et al. 2015, A&A, 574, A61
Liu, Z.-W., Röpke, F. K., & Han, Z. 2023, RAA, 23, 082001
Livio, M., & Riess, A. G. 2003, ApJL, 594, L93
Lundqvist, P., Kundu, E., Pérez-Torres, M. A., et al. 2020, ApJ, 890, 159
Lundqvist, P., Mattila, S., Sollerman, J., et al. 2013, MNRAS, 435, 329
Marcowith, A., Bret, A., Bykov, A., et al. 2016, RPPh, 79, 046901
Matteucci, F., & Recchi, S. 2001, ApJ, 558, 351
McMullin, J. P., Waters, B., Schiebel, D., Young, W., & Golap, K. 2007, in ASP Conf. Ser., 376, Astronomical Data Analysis Software and Systems XVIASP, ed. R. A. Shaw, F. Hill, & D. J. Bell (San Francisco, CA: ASP), 127
Mo, G., De, K., Wiston, E., et al. 2025, ApJL, 980, L33
Moore, K., & Bildsten, L. 2012, ApJ, 761, 182
Murphy, E. J., Bolatto, A., Chatterjee, S., et al. 2018, in ASP Conf. Ser., 517, Science with a Next Generation Very Large Array, ed. E. Murphy (San Francisco, CA: ASP), 3, https://ui.adsabs.harvard.edu/abs/2018ASPC..517....3M/abstract
Nadezhin, D. K. 1985, Ap&SS, 112, 225
Nomoto, K. 1982, ApJ, 253, 798
O'Dell, C. R., Sabbadin, F., & Henney, W. J. 2007, AJ, 134, 1679
Panagia, N., Van Dyk, S. D., Weiler, K. W., et al. 2006, ApJ, 646, 369
Perlmutter, S., Aldering, G., Goldhaber, G., et al. 1999, ApJ, 517, 565
Phillips, M. M. 1993, ApJL, 413, L105
Phillips, M. M., Lira, P., Suntzeff, N. B., et al. 1999, AJ, 118, 1766
Pskovskii, I. P. 1977, SvA, 21, 675
Raiteri, C. M., Villata, M., & Navarro, J. F. 1996, A&A, 315, 105
Reynolds, S. P., Williams, B. J., Borkowski, K. J., & Long, K. S. 2021, ApJ, 917, 55
Riess, A. G., Filippenko, A. V., Challis, P., et al. 1998, AJ, 116, 1009
Ruiter, A. J., & Seitenzahl, I. R. 2025, A&ARv, 33, 1
Salamanca, I., Cid-Fernandes, R., Tenorio-Tagle, G., et al. 1998, MNRAS, 300, L17
Seaquist, E. R., Krogulec, M., & Taylor, A. R. 1993, ApJ, 410, 260
Seaquist, E. R., & Taylor, A. R. 1990, ApJ, 349, 313
Sedov, L. I. 1959, Similarity and Dimensional Methods in Mechanics (Academic Press)
Sfaradi, I., Horesh, A., Fender, R., et al. 2025, ApJ, 979, 189
Sharma, Y., Sollerman, J., Fremling, C., et al. 2023, ApJ, 948, 52
Shen, K. J., Kasen, D., Miles, B. J., & Townsley, D. M. 2018, ApJ, 854, 52
Silverman, J. M., Nugent, P. E., Gal-Yam, A., et al. 2013, ApJS, 207, 3
Smith, N. 2014, ARA&A, 52, 487
Soderberg, A. M., Chevalier, R. A., Kulkarni, S. R., & Frail, D. A. 2006, ApJ, 651, 1005
Soderberg, A. M., Kulkarni, S. R., Berger, E., et al. 2005, ApJ, 621, 908
Soderberg, A. M., Margutti, R., Zauderer, B. A., et al. 2012, ApJ, 752, 78
Tang, X., & Chevalier, R. A. 2017, MNRAS, 465, 3793
Taylor, G. I. 1946, RSPSA, 186, 273
Terwel, J. H., Maguire, K., Dimitriadis, G., et al. 2025, A&A, 694, A11
Thompson, T. A., Quataert, E., & Murray, N. 2009, MNRAS, 397, 1410
Tutukov, A. V., & Yungelson, L. R. 1979, AcA, 29, 665
Virtanen, P., Gommers, R., Oliphant, T. E., et al. 2020, NatMe, 17, 261
Wang, L., Hu, M., Wang, L., et al. 2024, NatAs, 8, 504
Webbink, R. F. 1984, ApJ, 277, 355
Weiler, K. W., Panagia, N., Montes, M. J., & Sramek, R. A. 2002, ARA&A, 40, 387
Whelan, J., & Iben, I. J. 1973, ApJ, 186, 1007
Wood-Vasey, W. M., & Sokoloski, J. L. 2006, ApJL, 645, L53
Yang, X., Liu, Z., Shan, H., et al. 2023, ATel, 16080, 1